Multifunctional ZnO nanorod-reduced graphene oxide hybrids nanocomposites for effective water remediation: Effective sunlight driven degradation of organic dyes and rapid heavy metal adsorption

Kuglaur Shanmugam Ranjith [a,*], Palanisamy Manivel [b], Ramasamy Thangavel Rajendrakumar [c], Tamer Uyar [a,*]

[a] Institute of Materials Science & Nanotechnology and UNAM–National Nanotechnology Research Center, Bilkent University, Ankara 06800, Turkey
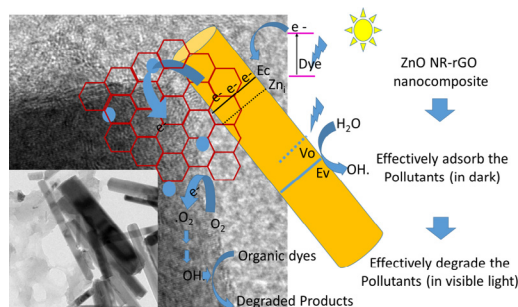[b] Centre for Nanoscience and Nanotechnology, School of Physics, Bharathidasan University, Tiruchirappalli 620 024, Tamil Nadu, India
[c] Department of Nanoscience and Technology, School of Physics, Bharathiar University, Coimbatore 641 046, Tamil Nadu, India

HIGHLIGHTS

- Feasible design and interface improvise the catalytic behavior of nanocomposites.
- Distinctive features enhances the structural functionality and carrier separation.
- Tunable electro negative functionality of rGO favors the absorption site over ZnO.
- Vital role behind the light absorption were favored by rGO ratio with ZnO.

GRAPHICAL ABSTRACT

ARTICLE INFO

ABSTRACT

We demonstrate the multi-functionality engineering on nanocomposite by combining one dimensional (1D) ZnO nanorod (NR) and two dimensional (2D) reduced graphene oxide (rGO) for efficient water remediation. Nano-engineered ZnO NR-rGO nanocomposites show efficient water remediation in terms of degradation of organic dyes and removal of heavy metal ions. Herein, we report on the fabrication of ZnO NR-rGO nanocomposite via a facile template-free hydrothermal route with an aim to improve the visible photocatalytic efficiency of the ZnO NR based nanocomposites. The structural and morphological features reveal that the rGO sheets are attached on the ZnO NRs and form a hybrid composite assembly. The surface enabled ZnO NR-rGO nanocomposites were used to degrade organic dye molecules (methylene blue (MB), methyl orange (MO) and rhodamine B (RhB)) under visible irradiation and adsorb Cu (II) and Co (II) ions from water through an adsorption process. The nanocomposite containing 7.5 wt% rGO and ZnO NRs shows a 4-fold enhancement in the visible photocatalytic activity and effective removal of Cu (II) and Co (II) ions from aqueous solution respectively. The photocatalytic performance is discussed in detail with respect to interaction between ZnO NRs and rGO sheets, light-harvesting properties of the nanocomposites. The effective experimental adsorption data also fit very well with the pseudo-second-order model which reveals the surface adsorption of metal ions. The results provide insight into a new method utilize for both visible photo degradation and adsorption for the removal of various wastewater pollutants. Construction of hybrid form of nanostructures delivers the effective catalytic properties with tunable functionalities for the water remediation.

© 2017 Elsevier B.V. All rights reserved.

---

* Corresponding authors.
  E-mail address: uyar@unam.bilkent.edu.tr (T. Uyar).

1. Introduction

Environmental water pollution caused by organic pollutants and heavy metals have become a serious problem worldwide that threatens the balance of nature and the sustainable endurance of human beings [1,2]. Most organic pollutants existing in trace or even ultra-trace quantities in the environment would be toxic and could accumulate along the food chain which may lead to serious ecological and health hazards. In order to eliminate the hazardous heavy metals and organic pollutants in wastewater, various photocatalytic semiconductor materials, such as TiO_2, ZnO, CdS, Fe_2O_3 etc. were used in contiguous years [3,4]. Meanwhile, wideband gap semiconductors such as TiO_2 and ZnO are promising photocatalysts but they hinder the effective absorption of visible light in photocatalytic process [5]. In order to bring the wide band gap semiconductor active in visible photo energy, various materials have been employed as effective change extractor through hybrid hetero structural interface [6]. One dimensional (1D) metal oxide nanostructured materials such as nanofibers, nanotubes, and nanorods are particularly interested as catalysts, owing to their large surface to volume ratio, efficient electron transport and ability to generate more reactive oxygen species on the surface [7]. Meanwhile, heavy metal removal on semiconducting nanostructures was investigated through colorimetric and fluorescence chemo sensing process [8,9]. Despite their independent advances, a system integrating both the rapid removal and effective degradation of organic pollutants remains largely unexplored. A rationally designed material with such feature could greatly enhance the versatility of the functional devices, improve the efficiency and reduce the water treatment cost. The fine grain size of the metal oxide nanostructures favor the aggregation by the Van der walls force or electrostatic interaction and it's minimize the adsorption ability, stability and selectivity [4,9]. To overcome this technical bottleneck, some researcher's immobilized nanometer-sized metal oxides on different carbon based materials such as activated carbon (AC), carbon nanotubes (CNTs) and graphene in order to improve its functional properties [10]. In the carbon family, graphene has an attractive two-dimensional single-layer sheet of sp^2-hybridized carbon atoms, possesses excellent charge carrier and electron mobility, which leads to effective separation of photo-generated carriers with high surface area, excellent thermal conductivity, and high electronic conductivity, and optically transparency [11]. Recently, the combination of oxide semiconductor and graphene functiona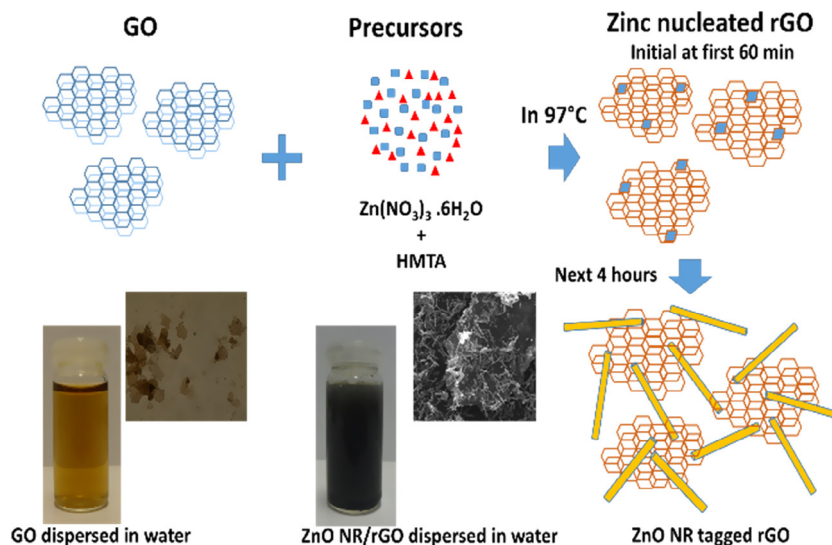lities including TiO_2, ZnO, CuO, MnO_2, Fe_2O_3, $CoFe_2O_4$, $MnFe_2O_4$ has been demonstrated to effectively improve the photocatalytic activities in these composite systems [12]. The primary role of graphene in these composite semiconductor photocatalyst systems is to delocalize the photogenerated electron through its π network, which inhibits the recombination process and hence improves the photocatalytic performance. Chen et al. [13] indicated that carbon based iron oxide magnetic composites could be employed as an effective adsorbent for the adsorption of Ni(II) and Sr(II) from wastewater. The adsorption capacity of the composites was determined to be much higher than that of metal oxides. Graphene possesses similar physical properties to CNTs but has larger surface areas than the latter. Construction of photo active 1D nanostructures over the two dimensional (2D) carbon based structures offers the promising photoactivity and effective charge separation efficiency with improvised surface functionality. By grafting over the elongated 1D nanorods on 2D graphene nano sheet were furnish a new form of nanocomposite system and its offer a facile and continuous, directionated electron flow with numerous reaction sites, stability and highly efficient catalytic properties [14,15].

In this current study, the ZnO nanorods (NRs) on reduced graphene oxide (rGO) nanocomposites (ZnO NR-rGO) were prepared by simple grafting of or growth of ZnO NRs in a homogeneously dispersed GO solution and subsequent drying (Scheme 1). ZnO NR-rGO samples were tested for degradation of the organic dye molecules such as methylene blue (MB), methyl orange (MO) and rhodamine B (RhB) and also for the adsorption of Cu (II), Co (II) ions from aqueous systems. This work not only demonstrated the possibility and validity of ZnO NR-rGO nanocomposite as promising adsorbents for pollutant removal and environmental remediation, but also gives insight into understanding the catalytic and adsorptive behavior of ZnO NR-rGO nanocomposite. We demonstrated that the grafted of 1D ZnO NR catalysts on both sides of a 2D rGO scaffold form a charge transportable network and result in enhanced catalytic activity and improved adsorptive nature. The kinetics of the process was also very well examined by fitting the experimental data with theoretical models.

2. Experimental section

2.1. Materials

Graphite flake, sodium nitrate ($NaNO_3$), potassium permanganate ($KMnO_4$), zinc nitrate hexahydrate ($Zn(NO_3)_2 \cdot 6H_2O$),

Scheme 1. Illustration of the synthesis processing of ZnO NR-rGO nanocomposite bridges.

hexamethylenetetramine (HMTA), copper chloride (CuCl$_3$) and cobalt chloride (CoCl$_3$), rhodamine B (RhB), methyl orange (MO), methylene blue (MB), nitric acid (HNO$_3$), sulfuric acid (95%, (H$_2$SO$_4$)) and ethanol (C$_2$H$_5$OH) were purchased from Sigma Aldrich. Polyethyleneimine (PEI) were acquired from Scientific Chemical Reagent Co, Ltd. All chemicals were analytical grade. The solvent used in this study is deionized and doubly distilled water.

2.2. Preparation of ZnO-rGO nanocomposites

Graphene oxide (GO) was synthesized from natural graphite flakes by a modified Hummers method [16]. The 1D ZnO NRs were synthesised through the aqueous solution using equal mole of (0.125 mM) Zn(NO$_3$)$_2$·6H$_2$O and HMTA [17]. The clear experimental procedures for synthesis of GO and ZnO NRs were given in supporting information part. In a typical synthesis, 20 mL of deionized water containing specific weight ratio of GO was added in ZnO NR growth precursor solution. After stirring for 30 min, the mixed solution was transferred into a 100 mL autoclave with a Teflon liner, which was kept at 140 °C for 4 h and then cooled to room temperature naturally. The products were rinsed thoroughly with distilled water and ethanol and annealed under nitrogen atmosphere at 150 °C for 4 h. Other samples were synthesized via the same procedure with different weight ratio of GO flakes to ZnO NRs. After the hydrothermal process, GO were thermally reduced and form the ZnO-rGO based nanocomposites. The as-obtained composites were labelled based on the weight ratio of GO to ZnO in precursor materials. For example, GZ2.5 means that the 2.5 wt % of GO with ZnO (∼350 mg). As per that 2.5, 5.0, 7.5, 10.0, 12.5 wt% of GO added ZnO nanocomposites were named as GZ2.5, GZ5.0, GZ7.5, GZ10.0 and GZ12.5, respectively.

2.3. Adsorption kinetics of dye molecules

The batch mode adsorption studies for RhB were carried out by an agitating photocatalyst in dye solution at 25 °C. Typically, 50 mL of RhB (10 mg/L) aqueous solution and 25 mg of photocatalyst (ZnO, GZ7.5 and GO) were added into a beaker and agitated in the dark. Then, aliquots (1 mL) were withdrawn at specific time intervals to determine solution concentrations. The concentrations of various dyes were monitored using UV−vis absorption spectrophotometer at 525.5 nm for RhB. The equilibrium adsorption capacities of dyes onto photocatalysts were determined according to the following formula:

$$Q_e(mg/g) = ((C_o - C_e)V)/M \qquad (1)$$

where Q$_e$ (mg/g) is the equilibrium adsorption capacity of the adsorbent, C$_0$ and C$_e$ (mg/L) are the initial and final concentrations of dyes, respectively, V (L) is the volume of the original mixture, and M (g) is the weight of photocatalyst added.

2.4. Photocatalytic degradation measurements

The photocatalytic degradation experiments for RhB, MO, and MB were carried out in a self-prepared reactor. In the degradation procedure, 50 mg catalysts were immersed in a 150 mL beaker containing 100 mL of RhB, MO, MB and aqueous solution (10 mg/ L). The solution was irradiated by a 75 W xenon lamp (visible light with UV cut off filters) and natural sunlight with UV cut off filter (Lee type 226 (USA)). For sunlight irradiation, samples were irradiated on a normal sunny day between 9.00 a.m. and 4.00 p.m under the shadows in order to avoid the evaporation of solution through heat effect. The light intensity was the constantly checked every 30 min using the lux meter. The adsorption-desorption equilibrium was attained by 50 min stirring in a dark room. The vertical

distance between the solution level and the horizontal plane of the lamp was fixed at 10 cm. At an interval of 30 min, 3 mL of solution was taken out from the reactor. The absorbance of the solution was determined using a UV–Vis absorption photometer at the characteristic absorption wavelength (661 nm, 542.5 nm and 464.5 nm for MB, RhB and MO respectively). The degradation efficiency of dyes by the photocatalysts was determined according to the following formula:

$$\eta\% = ((C_o - C_e)/C_e) \times 100 \qquad (2)$$

where η (%) is the degradation efficiency, C$_0$ and C$_e$ (mg/L) are the initial and final concentrations of dyes, respectively.

2.5. Sorption studies

The Cu (II) and Co (II) adsorption process was executed for pure ZnO NR and rGO on ZnO adsorbents to determine the optimum adsorption conditions. A typical batch mode adsorption experiments were carried out with ZnO NR-rGO nanocomposite adsorbent at room temperature. The effect of pH on the adsorption capacity (Qo) was investigated in the range from 2 to 10 by using Cu (II) and Co (II) solution prepared from the standard 100 mg/L stock solution to the preferred concentration of 10 mg/L through sequential dilution. The pH was adjusted by using sodium hydroxide (NaOH) or hydrochloric acid (HCl) solutions. The resultant mixture solutions were transferred to 50 mL standard measuring flask and stirred on a thermostatic mechanical shaker operating at a constant speed of 300 rpm. Finally, the sample was withdrawn from the shaker at predetermined time intervals and the supernatant was collected by centrifuging at 5000 rpm for 3 min. The resultant clear solution was used to estimate the Cu (II) and Co (II) adsorption by using spectrophotometric analysis. The supernatant solution of 20 mL was taken in a test tube and 2 mL of polyethyleneimine solution (0.94 mg/mL) was added. This was further incubated for color development and finally the absorbance of the samples was measured in a UV–visible spectrophotometer in the wavelength of 275 nm and 315 nm for Cu (II) and Co (II) ions respectively [18].

2.6. Materials characterizations

The structure, microstructure and morphology of the as obtained samples were characterized by X-ray powder diffraction (PANalytical X'Pert multipurpose X-ray diffractometer) with Cu Kα radiation (λ = 1.54056 Å), Raman spectroscopy (in Via-Reflex, Renishaw, U.K.), field-emission scanning electron microscopy (FE-SEM, Quanta, FEG 250), transmission electron microscopy (TEM, FEI-Tecnai G2 F30), Fourier transform infrared spectroscopy (VER-TEX 801 HYPERION 2000, Bruker Optics, Germany). X-ray photoelectron spectroscopy (XPS, Thermo K-alpha-monochromated) was employed to analyze the surface chemical composition. The diffused reflectance and fluorescence spectra of the samples were taken at room temperature on a UV–visible spectrophotometer (UV3600, Shimadzu, Japan), and photoluminescence (PL) spectro fluorometer (time-resolved fluorescence spectrophotometer (FL-1057 TCSPC) with an excitation at 325 nm. The absorbance spectra of organic pollutants and heavy metal ions were obtained by using UV–vis Spectrophotometer (Varian Cary 100). The chromatic experiment with HPLC-UV/vis system were carried out on liquid chromatograph mass spectroscopy (Agilent Technologies 6224 TOF) using binary solvent gradient pump and automatic sample injector. The specific surface area of the samples were analysis using Brunauer-Emmet-Teller (BET) method carried out on Micromeritics Tristar analyser after degassing the samples for 3 h at 200 °C.

3. Result and discussion

3.1. Structural and morphological studies

The typical X-ray diffraction (XRD) patterns of the GO, ZnO NR and GZ composites (GO loading level: 2.5 wt%, 7.5 wt% and 12.5 wt%, respectively) were shown in Fig. 1. It can be observed from the XRD pattern that the as prepared GO shows a sharp peak at $2\theta = 10.6°$, corresponding to the (0 0 1) reflection of GO. From Fig. 1, all the diffraction peaks of the pure ZnO and ZnO NR-rGO composites (GO loading level: 2.5 wt%, 7.5 wt% and 12.5 wt%) synthesized can be matched with hexagonal ZnO (JCPDS 36-1451). In the case of ZnO NR-rGO, the major diffraction peaks are consistent with pure ZnO phase and the broad diffraction peak assigned at 24.5° is attributed to the (0 0 2) plane of typical rGO. The d (0 0 2) peak near 24.5° is related to the stacking layers along the c-axis of reduced graphene oxide [19]. And it indicates that GO is simultaneously reduced to reduced graphene oxide at the temperature influence during the formation of ZnO NRs

Fig. 2 shows the FESEM and TEM images of as prepared GO, pure ZnO NRs and sample GZ7.5. Inset of the Fig. 2a shows the optical image of the GO reveal that the flakes with average size distribution of 5–10 μm and were observed to be composed of a few layers (Supportive information, Fig. S1). FESEM image of graphene oxide (Fig. 2a) shows the folded nature of the sheets. Fig. 2b shows the TEM image of few layered, wrinkled and folded GO. Insert shows the SAED of GO with diffused diffraction ring pattern which represents the disordered structure of GO due to the chemical oxidation on the conjugated graphite structure. In Fig. 2c, the hydrothermally

grown ZnO NRs are in the prismatic form, with length of 2–3 μm and the diameter of 100 nm. High-resolution transmission electron microscopy (HRTEM) lattice fringes of a single NR shows the oriented growth along the c axis [0 0 0 1] direction with lattice spacing of 0.26 nm representing (0 0 2) axis [20]. FESEM and TEM images of GZ7.5 reveal a well-defined attachment of ZnO NRs on rGO flakes which reveal the formation of ZnO NR-rGO nanocomposite from submicrometer to several micrometers (Fig. 2e). In the meantime, the ZnO NRs in the GZ7.5 are viewed to be wrapped in the interior of the pore walls which consists of thin layers of stacked rGO sheets (Fig. 2f). TEM observation further confirms the even distribution of ZnO with the wrapped interface with rGO sheets (Fig. 3).

Fig. 3 shows the TEM images of GZ7.5 which reveals that the ZnO NRs are intimately attached on the rGO sheet surface and distributed, with no morphological changes after the combination with rGO sheets via hydrothermal treatment. From the TEM images, it shows the presence of wrinkles and ripples and scrolls on the ZnO NR and rGO suggests the occurrence of few layered rGO sheets. Inset of the Fig. 3b and c, spotted pattern of the selected area electron diffraction (SAED) pattern of rGO reveal that rGO, employed as a reference, was observed to be composed of a few layers [21] (Fig. S2). As a function of initial hydrothermal process, ZnO nuclei were attached over the rGO and exhibit the presence of ZnO NRs progressively grown on the rGO flakes (Fig. S3 and Fig. 2f) which reveals the nucleation sites anchoring the ZnO NR on the rGO flakes during the growth process. However, SAED image of rGO showed set of six-fold symmetric diffraction points of a typical hexagonal configuration represents the thermal reduction of GO [19]. The specific BET surface area of the ZnO NR and ZnO NR-rGO (GZ7.5) nanocomposites were determined to be 2.336 m^2/g and 19.434 m^2/g, respectively. From the comparative isotherm results (Fig. S4), the decoration of rGO on the ZnO NRs apparently leads to an increase in the surface area as compared to the pristine ZnO NRs.

Raman spectroscopy was utilized to assess the existence and crystalline quality of rGO sheet in the ZnO NR-rGO nanocomposite (Fig. 4). For all composite specimens, two prominent characteristic peaks were observed at 334 and 435 cm^{-1}, correspondingly assigned as $E_2^{high} - E_2^{low}$ and E_2^{high} modes of the crystalline ZnO, respectively [22]. The peak at 582 cm^{-1} is assigned to (LO) mode, attributed to oxygen deficiency defects in ZnO [23]. The peak at 1130 cm^{-1} is due to the multiple-phonon scattering processes [24]. The intensity of these peaks is reduced in composites as compared to that in ZnO due to the interaction between ZnO and rGO. In addition, at higher wavelength the peak should observed at ~1140 cm^{-1} assigned to the 2LO vibrations which is due to the second order raman process [25]. Fig. 4(b–d) shows the Raman spectrum of GO and GZ composites. The G band at 1577 cm^{-1} is assigned to the E2g phonon mode of C sp2 atoms and the D band at 1336 cm^{-1} is a breathing mode of k-point phonons of A1g symmetry, originating from the defects. The intensity ratio (I_D/I_G) of the D band to the G band of GO is 0.801, which is the measure of Raman vibrations, expressed by the sp3/sp2 carbon ratio. For the ZnO NR-rGO hybrid composite samples, two broad peaks corresponding to the D and G band and the band intensity ratio was estimated as ~1.06. The peak intensity ratio were consistent with typical rGO, indicating that rGOs coexisted with ZnO NRs. Compared to GO, the hybrids exhibit a slight increase in the I_D/I_G ratio, which is due to the presence of more defects and the interaction between rGO and ZnO NRs [26]. The results indicate that ZnO NR-rGO nanocomposite were successfully prepared which was correlated with XRD results.

3.2. Optical studies

The UV–vis DRS absorption spectra of the ZnO NR-rGO nanocomposites are shown in Fig. S5a. The pure ZnO shows a sharp
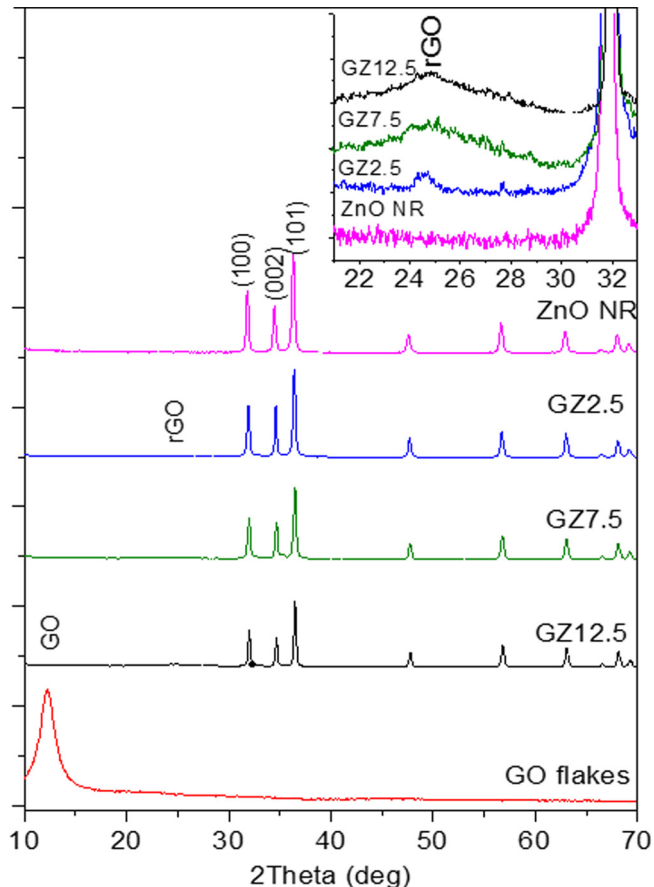

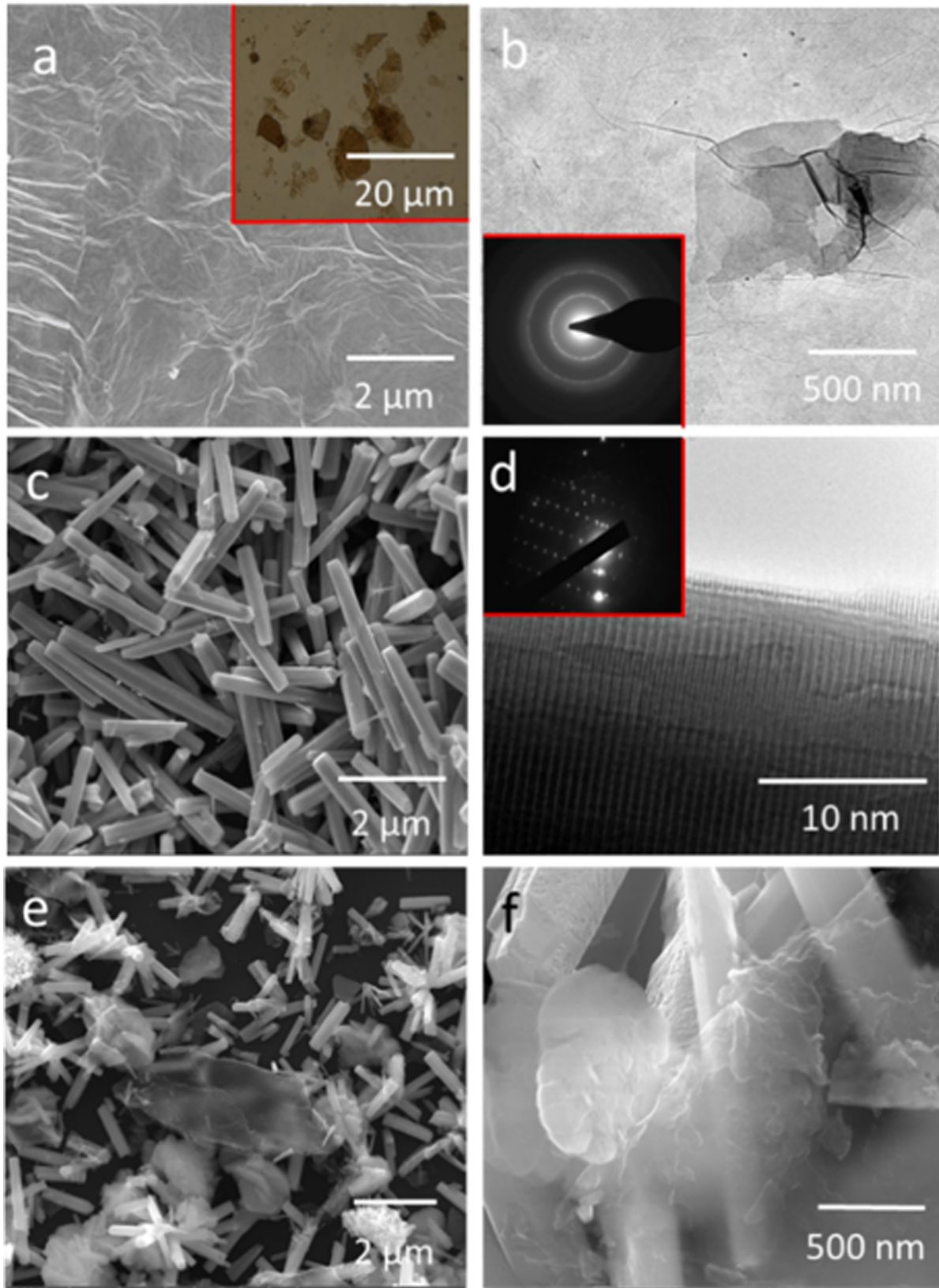**Fig. 1.** The XRD patterns of ZnO NR, GO, GZ2.5, GZ7.5 and GZ12.5 nanocomposite samples.

Fig. 2. FESEM (a) and TEM (b) images of GO synthesized by modified Hummers method. The insert of (a) and (b) corresponds to the optical images and SAED pattern of GO, respectively. SEM (c) and TEM (d) images of the ZnO NR formed by the hydrothermal process. The insert in (d) is the corresponding SAED pattern of ZnO NR. FESEM (e) image of GZ7.5 and high magnification FESEM (f) image of GZ7.5 nanocomposites.
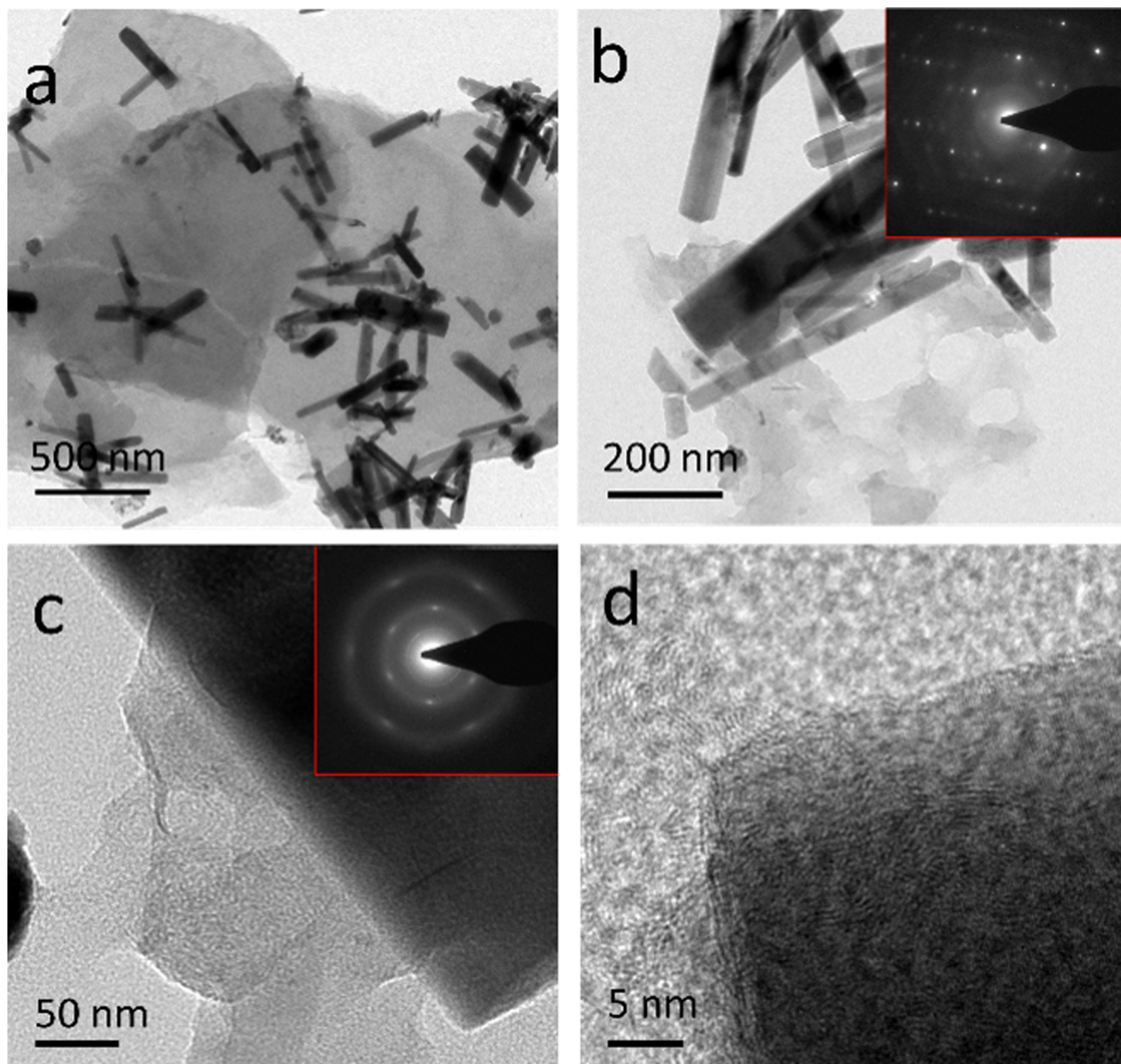
Fig. 3. (a, b) TEM and (c, d) HRTEM micrographs of the GZ7.5 nanocomposites. Inset show the SAED of the respective images.

absorption at 384 nm and the ZnO NR-rGO nanocomposite show the enhanced absorption in the visible region (400–800 nm) in addition to the absorption edge at 380 nm. The ZnO NR-rGO hybrids possess an intense and broad range of absorption in the visible region due to the presence of rGO. Compared to pure ZnO, the absorption intensity of GZ samples are reduced. With the increased mass ratios of rGO sheets, the absorption background of ZnO NR-rGO nanocomposite increase in the visible light range, which is ascribed to the black body effects of rGO sheets [26]. PL spectra provide useful information for the investigation of the interface charge carrier transfer and photogenerated electron–hole recombination process in ZnO NR-rGO nanocomposite system. Fig. 5 shows the room temperature photoluminescence spectra of pure and hybrid composites. All the samples exhibits the prominent sharp emission at 369 nm and 387 nm which attributes to the band edge emission and the Zn interstitial trap states related band below the conduction band and a broad emission at 550 nm which related to the oxygen related defect states [27]. The raised broad violet emission around 419 nm is probably due to the radiational defect related to the interfacial traps existing at the interface and emitted the radiation transition. The broad emission at 550 nm assigned to the trap-state emission result from

the intrinsic defects and vacancies of ZnO, such as interstitial oxygen and oxygen vacancies [28]. Hydrothermally grown ZnO NRs have the broad and promising defect related emission which was found to be composed of two major Gaussian components (Fig. S6) centered at 540 and 580 nm. The small 540 and 580 nm component can be related to the singly and doubly charged oxygen vacancy states (Vo^+ and Vo^{++}), respectively [29]. Compared with pure ZnO NRs, a significant depression in the PL emission was observed on introducing the rGO with the ZnO as the form of ZnO NR-rGO nanocomposite. This depression became more noticeable as the rGO mass ratio increased, suggesting the successful electron transfer from ZnO to rGO with the suppressed recombination process. This phenomenon supports the argument that the rGO acted as an effective electron scavenger for ZnO, leading to the pronounced charge separation observed for the ZnO NR-rGO nanocomposite. Decrease in the fluorescence yield of composite; suggest an additional pathway for the disappearance of charge carriers because of the interaction between excited ZnO NRs and rGO sheets. For the higher wt% of ZnO NR-rGO nanocomposite, emission peaks in the violet region are observed. It may due to trap state emission over the interface which promotes the Zn interstitial based defect emission or the peaks related due to the decay of exci-
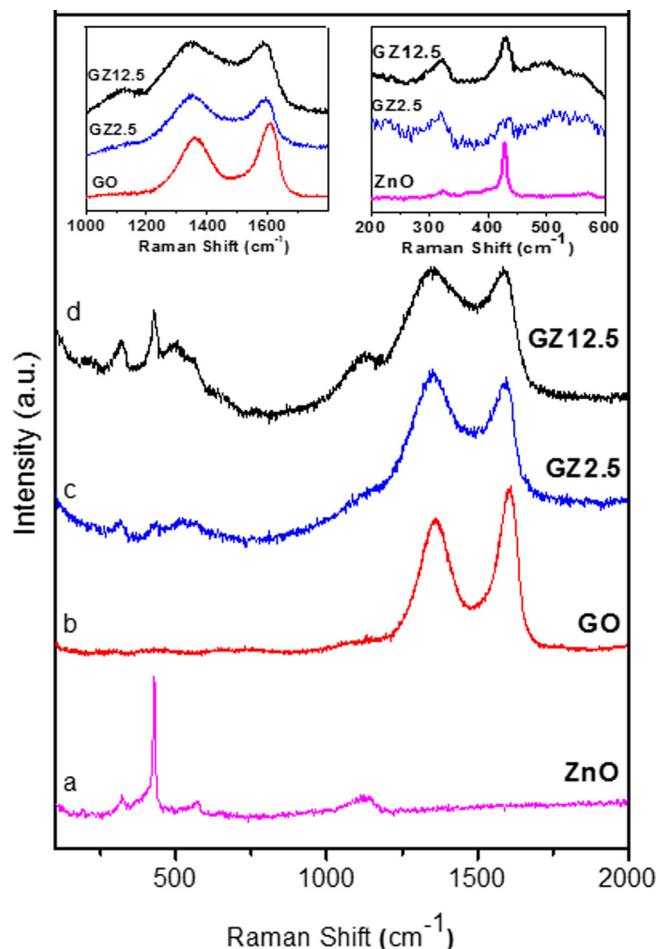
Fig. 4. Raman spectra of ZnO NR, GO, GZ2.5 and GZ12.5 nano composite samples.
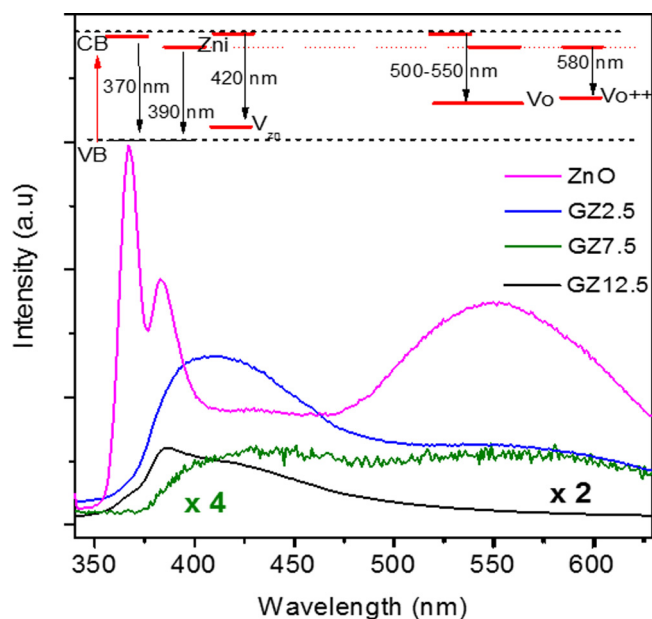

Fig. 5. Photoluminescence spectra of ZnO NR-rGO hybrid nanocomposites compared to pure ZnO NRs synthesized by hydrothermal method.

tons [30] from the LUMO of the graphene layer with an epoxy bond to the ZnO valence band.

The XPS full-scan survey spectrum shows the principal C1s, O1s, and Zn2p core levels in Fig. 6a. Inset shows the high resolution Zn

2p3/2 peak position of ZnO NR and GZ7.5 nanocomposites and the $Zn2p^{3/2}$ and $Zn2p^{1/2}$ main peaks with a difference of 23.1 eV shown in the Fig. S7a imply the characteristic peaks of Zn^{2+} [28]. However the shift to a higher binding energy by the 0.8 eV signifies the increase in the oxidation state of Zn, resulting from the contact with the electronegative reduced graphene [31]. This indicated the strong dipole interaction between the electro negative rGO and ZnO NRs. By comparing the peak intensity of O1s between ZnO and GZ samples, which reveal that the defect levels were turned on after tagging the ZnO and GO (Fig. 6b). By fitting the oxygen related band in the ZnO NR-rGO nanocomposite system by Gaussian function, it has been split into 4 set of peaks such as O ion in ZnO lattice (O_L) (530.1 eV), O ions in oxygen-deficient lattice in ZnO (O_V) (531.1 eV), chemisorbed oxygen species (O_C) (532.4 eV) and band interaction of C—O in rGO at 533.4 eV. Hydrothermally synthesized ZnO NRs have prominent O_V ratio which is equivalent to the O_L. While decorating the rGO with ZnO, O_V ratio reduced due to the oxidization of ZnO by the electronegative rGO with the increased functionality of chemisorbed oxygen species. A peak at 533.42 eV is observed for ZnO NR-rGO nanocomposite, which is attributed to the C—O band in rGO.

The reduction of GO after the hydrothermal process was further confirmed by the XPS C1 s spectra (Fig. 6c). As shown in Fig. 6c, the C 1 s XPS spectra of GO and GZ7.5 contained four deconvolution peaks at 284.5, 286.7, 287.5 and 289.1 eV, which represented C—C, C—O, C=O and O—C=O bonding, respectively. In brief, from the C1s XPS spectra of GO (Fig. 6c), a considerable degree of oxidation with four components that corresponds to carbon atoms in different functional groups can be seen: the non-oxygenated ring C, the C in C—O bonds, the C in C=O bonds and the carboxylate carbon (O—C=O) [32]. After hydrothermal process with the ZnO NRs, a notable decrease in oxygen content is clearly visible; in addition, the peak corresponding to the C=O bond has disappeared. The oxygen loss mainly results from the suppression of C—O peak, and the relative ratio of C(O) OH decreases remarkably as well. For the GZ7.5, an essentially low O-bound C content was obtained (23.91% for GZ7.5), as compared with the as prepared GO flakes (approximately 49.12%) indicating that the oxygen containing groups were significantly removed in the hydrothermal process [33]. More importantly, the low O-bound C content of the present ZnO NR-rGO nanocomposite ensures the occurrence of pronounced charge separation, which is crucial to its resultant photocatalytic performance. Fig. 6d shows the FTIR spectra of GO, ZnO NR, and GZ7.5. The broad absorption band at 3425 cm^{-1} is assigned to the hydroxyl groups of absorbed H_2O molecules. The absorption band at 450 cm^{-1} of GZ7.5 is similar to that of pure ZnO, which is attributed to stretching models of Zn-O. There is an obvious decrease in the intensities of oxygen functional group peaks in GO centered at 1071 cm^{-1} (C—O stretching), 1182 cm^{-1} (C—O—H deformation vibrations), and 1730 cm^{-1} (C=O stretching of COOH groups) vibration peaks in GZ7.5 compared to those in GO, indicating reduction of oxygen-containing groups of GO in the ZnO NR-rGO nanocomposite system [34]. The peak at 1615 cm^{-1} can be assigned to the skeletal vibrations of unoxidized graphitic domains. However, all these bands related with the oxygen functional groups almost disappear or appear with significantly lower intensities in the FTIR spectra of the GZ nanocomposites. These results confirm that these oxygen functional groups are almost removed in the process of thermal functionalization, and the GO is reduced to a great extent.

3.3. Photocatalytic degradation

Pure ZnO NRs exhibit a nearly negligible adsorption (less than 5% in 3 h) for organic pollutants (Fig. 7a). For GO the adsorption efficiency for MB, RhB and MO are 27.8, 23.3, and 17.3% after 3 h
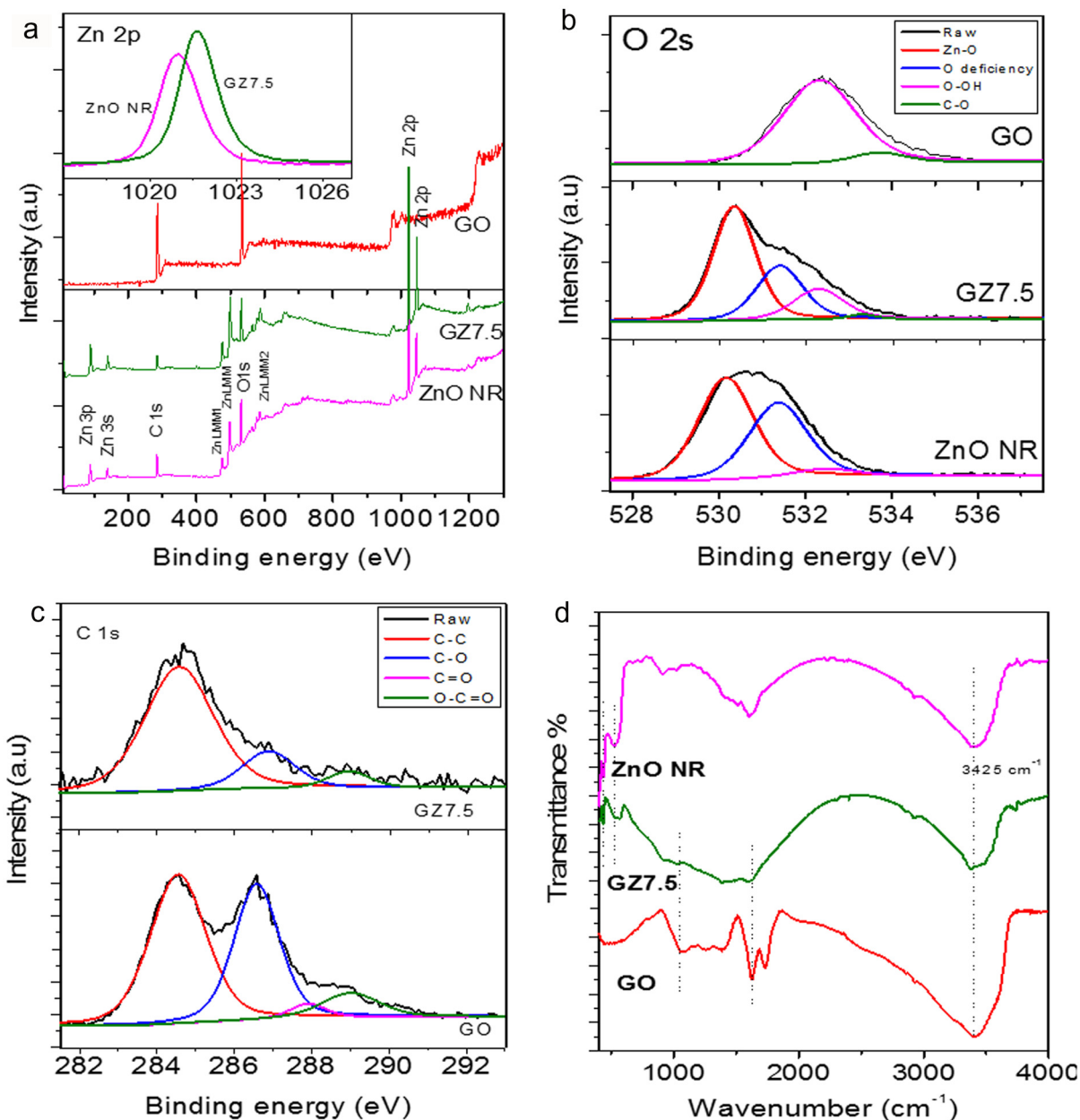
Fig. 6. (a) XPS survey spectra of ZnO NR and GZ7.5 nanocomposite. High-resolution XPS spectrum of Graphene composites (b) O 2s and (c) C 1s patterns and (d) FTIR spectra of ZnO NR, GZ7.5 and GO respectively.

and the GZ12.5 samples propose the adsorption rates for MB, RhB and MO are 15.8, 13.3, and 10.2% respectively, (Fig. 7a) all of which are much higher than those of pure ZnO NRs. After the introduction of rGO, the adsorption rates are greatly enhanced due to its higher specific surface area. Prior to irradiation, the photocatalytic reaction system was magnetically stirred in the dark for 50 min to reach the adsorption/desorption equilibrium of dye molecules on the surface of the photocatalysts. Fig. 7b and c shows the degradation rate of RhB with ZnO and GZ composites under visible and natural sunlight irradiation, respectively. After 100 min of visible irradiation, the photocatalytic degradation efficiency of RhB for ZnO NR, GZ2.5, GZ5.0 GZ7.5 GZ10.0 and GZ12.5 are 25.9, 49.6, 59.8, 80.4, 43.5 and 37.2%, respectively, and except ZnO NR, all other GZ composites were promisingly active under visible irradiation. Clearly, GZ7.5 shows superior photo degradation rate (Fig. S8) of 0.0227 min^{-1} and 0.0258 min^{-1} under visible and natural sunlight irradiation which is 7 times higher than the pure

ZnO NRs. Fig. 7d shows that the photo degradation efficiency of MB, RhB and MO for sample GZ7.5 is 93.9, 88.08 and 75.3% after 180 min of irradiation, much higher than those of pure ZnO NR. This indicates that the introduction of rGO is greatly beneficial to the improvement of catalytic activity by work as a sensitizer in the photoreaction. For further study on photocatalytic mechanism (Fig. S9(a–c)) shows the batch experiment of photodegradation of MB, RhB and MO (initial concentration, 10 mg/L, 100 mL) with 50 mg of ZnO and GZ7.5 for various durations. About 80% of pollutants were removed in 90 min after visible illumination in presence of GZ7.5.

In contrast, only 20% was removed in presence of ZnO NRs. The degradation profile of different pollutants reveals that the cationic dyes such as MB and RhB interacted more with the hybrid system than MO and results in faster efficient degradation. This was due to the higher negative potential value in hybrid composites which favors the more absorbance rate for the cationic dyes than the
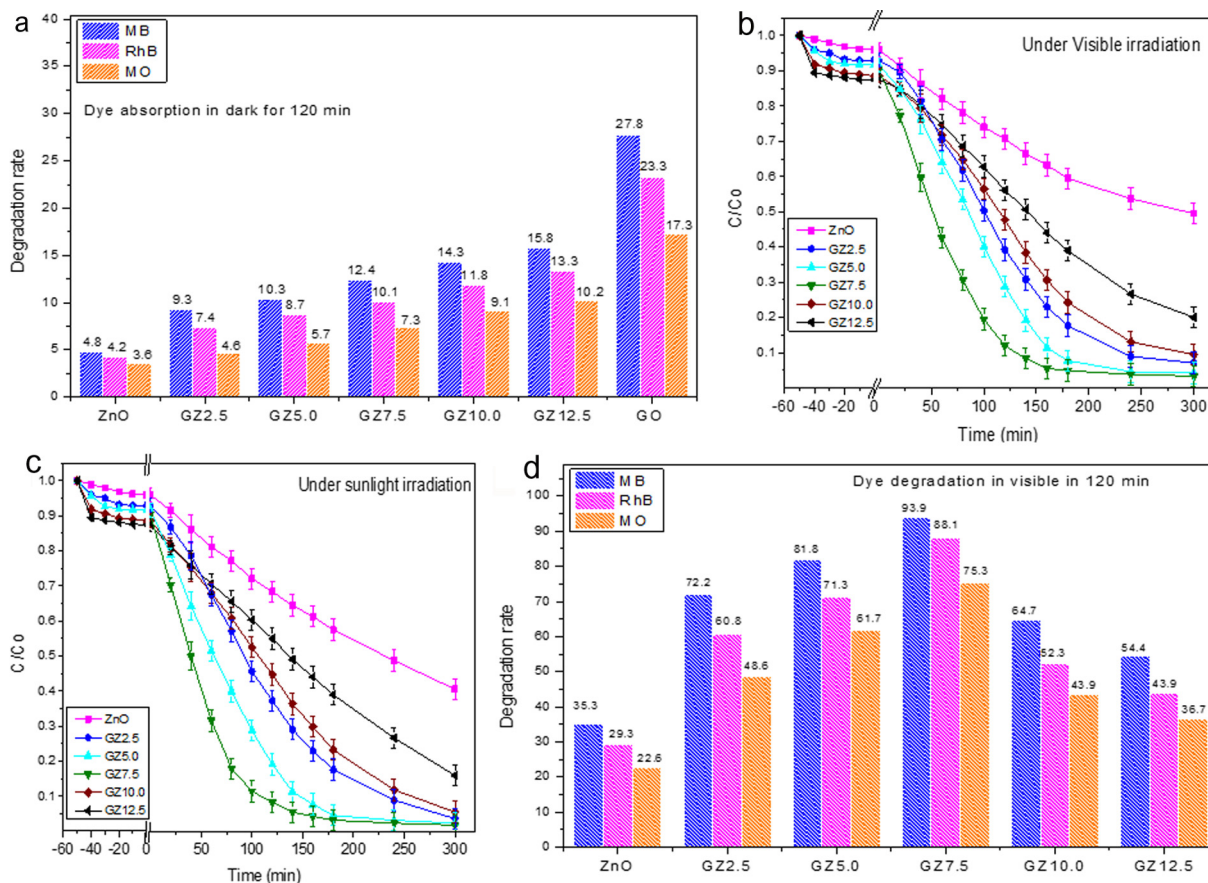
Fig. 7. Dye adsorption and Photocatalytic degradation of RhB for the pure ZnO NR and ZnO NR-rGO nanocomposite (a) Adsorption of MB in dark, (b) degradation under visible irradiation, (c) degradation under sunlight irradiation and (d) comparative degradation efficiency over different dye pollutants.

anionic dye, MO. In the cycling experiments for the photodegradation of RhB using GZ7.5, the degradation rate is as high as 92.4% after 10 cycles (Fig. S10), suggesting great stability of the photocatalyst. Additionally, as a control experiment catalytic performance of GZ7.5 were compared with the 7.5 wt% of GO-ZnO mixed composites (Fig. S11). The mixed form of catalyst exhibits the slower catalytic efficiency as compared with GZ7.5 which clearly reveals the contract interface and carrier transport between ZnO NRs and rGO are crucial factors to achieve higher photocatalytic activities. The dominant factor in order to improve the catalytic activity was that while grafting the ZnO NRs on the rGO surface, continuous conductive paths are built through the rGO, thereby effectively reducing the transfer resistance of photogenerated electrons and inhibiting the recombination of photogenerated electrons and holes. Further, on inducing the ZnO NR-rGO nanocomposite system, created interfacial electric field between the ZnO and rGO, thus improving the separation efficiency of photo induced electron-hole pairs. Due to the natural functionality of higher electron transfer ability in graphene based system, the lifetime of photo induced electrons and holes in the hybrid system improves. This indicates that it has great application potential nature.

While increasing the rGO dosage over GZ7.5, the catalytic efficiency starts to depress in the GZ10.0 and GZ12.5. This decrease in the catalytic behavior is believed to be due to overloading of rGO that act as a block that avoid the light absorption of ZnO and encourages the electron hole recombination [33]. Even though the effective absorption rate was high over the rGO dosage, decrease in the carrier separation efficiency results in the suppression of resultant catalyst and it may called as shield effect. Similar behavior on the effect of rGO dosage has been reported previously,

where excess of rGO caused a negative influence over the catalytic performance [35]. Additionally the dye molecules which we used has come sensitization effect which will give some charge carrier to the catalytic surface which can promotes the radical production to degrade the dye molecules under visible illumination [36]. But the possibility over the subsequent electron transfer from the excited dyes to the ZnO would be determined by the adsorption of dyes through the electrostatic interaction with the catalytic surface. At the neutral pH, ZnO has positively charged (point of zero charge of ZnO is at around $pH_{zpc} \sim 9$) and electrostatically it repels the cationic dyes. But the presence of rGO with the ZnO will favor the dye interaction and induces the possibility of sensitization effect. And according to the dosage of rGO with ZnO the dye absorption rate were increased in contrast to degradation rate (Fig. 7a). It reveals that, there is a possibility of dye sensitization effect but the effective degradation probabilities were determined by the carrier separation efficiency at the ZnO and rGO interface under visible irradiation.

On the basis of the above analyses, we propose that the improved photocatalytic activity of composites mainly results from the interaction of ZnO-rGO owing to the more efficient separation of electron-holes, and the improved optical absorption in visible light range. A possible reaction mechanism and the photo degradation process are illustrated in Fig. 8. Irradiated by the simulated visible photon energy, excited electrons in the ZnO NRs were extracted by the rGO bridges and high conductivity of rGO sheets enable quick charge transfer, thereby prolonging the lifetime of charge carriers and suppressing the recombination. The photoinduced electrons on ZnO surface and the trapped electrons on rGO sheets induce redox reaction and degrade the organic pol-
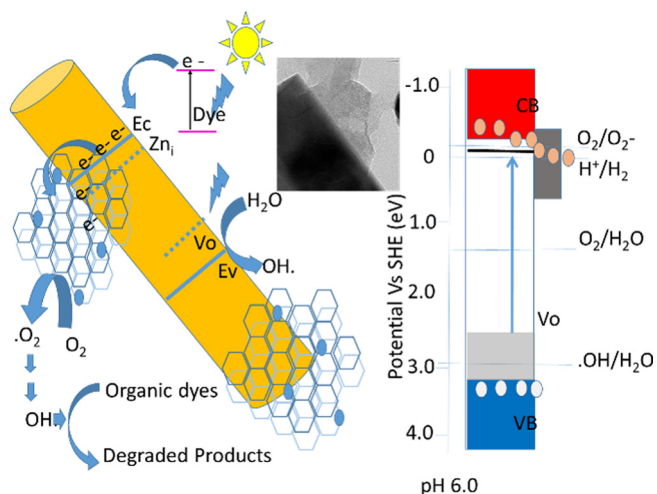
Fig. 8. Schematic and mechanism of photocatalytic degradation using ZnO NR-rGO nanocomposite hybrids.

lutants. Several mechanisms have been proposed to account for the photocatalytic behavior on the inorganic-organic based photocatalytic system [8,9,13,14,37]. We believe that excellent performance of GZ7.5 can be attributed by the aspects of both the surface interaction over the surface adsorbed molecules and the effective transfer of charge carriers. The visible catalytic ability and favorable higher interaction of rGO on the ZnO NR surface were investigated by analysing the degradation performance of the colorless 4-chlorophenol which provides evidences for the excluded dye sensitization effect and denotes the visible catalytic behavior through the rGO-ZnO nanocomposite formation (Fig. S12).

In general, dye based pollutant degradation mechanism could be explained by the electron-hole (e-h$^+$) separation between conduction and the valance band and the slow recombination rate of charge carriers in the ZnO system. During photo irradiation, separated carriers promoted the production of reactive oxygen species such as active hydroxyl (OH$\cdot$) and superoxide (O$_2$) radicals. These OH and O$_2$ have been considered as oxidative species and usually determine the degradation of various organic dyes under photo irradiation. Based on the proposed degradation mechanism, higher effective charge separation of ZnO NR-rGO nanocomposite sufficiently produces active oxygen radicals which are basically responsible for the degradation of organic dye molecules. Meanwhile, the rGO supported ZnO NR composite catalysts exhibits higher visible photocatalytic degradation efficiency than the ZnO NR. This may be due to separation of efficient carriers on the surface by rGO in the composite, thus delaying the recombination rate and effectively producing sufficient amount of O$_2$ species under photo irradiation. It is already reported that the oxygen radicals are produced as a result of rGO being grafted on the ZnO under photo irradiation and availability of sufficient amount of O$_2$ species followed by OH$\cdot$ production favors effective degradation of organic pollutants. Therefore, the heterogeneous catalyst ZnO NR-rGO nanocomposite network exhibits high degradation over organic dyes under visible light irradiation due to the generation of oxy-radicals on the surface. Further surface interaction of organic pollutants with π-π conjunction over the aromatic regions of rGO increases the adsorption rate of dye molecules than the pure ZnO NR surface. And these adsorbed pollutant molecules were more favorable in terms of interaction with reactive oxygen species than those in the solution form. The promoted interfacial electric field between the ZnO NR and rGO facilitates the separation of electro hole pairs and induced the faster carrier migration. And to further investigate the degradation sequence and the by-product formation during the catalytic

process, the degradation of MB dye molecules respective to time under visible irradiation with ZnO and GZ7.5 were analysed through the LC–MS measurements. LC–MS spectra (Fig. S13) of the degraded dye solution with respective to time clearly reveals the degradation of MB dye molecules without forming any by-products. After the irradiation of 180 min, the toxic dye molecules in the aqueous solution were completely degraded on using GZ7.5 as the catalyst.

3.4. Cu (II) and Co (II) adsorption

As the ZnO NR-rGO nanocomposite have the ability to adsorb organic pollutants, their efficiency in effective adsorption to remove heavy metals and hazardous materials from wastewater are investigated. ZnO NR and ZnO NR-rGO (GZ7.5) nanocomposites were employed for the Cu (II) and Co (II) adsorption ability in aqueous solution medium. The removal efficiency of the ZnO NR and ZnO NR-rGO nanocomposite were studied by varying the pH, initial concentration of the metal ions and contact time. Fig. 9a shows the effect of pH on the adsorption of Cu (II) and Co (II) ions from aqueous solution. The Cu (II) and Co (II) adsorption behavior of ZnO NR and ZnO NR-rGO nanocomposite was investigated by varying the pH from 2 to 10 in the adsorbent concentration of 100 mg/L with initial concentration of adsorbate as 20 mg/L and contact time of 180 min. The results show the adsorption capacity of Cu (II) is 7.1, 21.3, 63.3, 77.1 and 68.5% for ZnO NR in the pH of 2, 4, 6, 8, 10 respectively. For the ZnO NR-rGO (GZ7.5) nanocomposite bridges the adsorption efficiency was 9.7, 49.7, 96.4, 98.6 and 96.9% for the pH of 2, 4, 6, 8, 10 respectively.

Further investigations were carried out using Co (II) as representative. Results revealed that the adsorption percentage of Co (II) increased from 11.7% to 90.1% on varying the pH from 2 to 10 over the ZnO NR-rGO nanocomposite. The effect of contact time on the adsorption of metal ions was studied under neutral pH by adding 10 mg/L of adsorbent and 20.0 mL of sample solution into special glass stoppered tubes and the experiments were performed when the contact time varied from 10 to 120 min. Results were shown in Fig. 9b. It is evident that the adsorption of metal ions on ZnO NR-rGO nanocomposite is initially very fast (Fig. S14). In the present work, 120 min was selected as the contact time to ensure equilibrium. Sorption kinetics is an important aspect for defining the adsorption efficiency and is expressed in terms of the rate of solute removal that controls the residence time of the adsorbate in the solid-solution interface [38]. The kinetics of the removal of Cu (II) and Co (II) ions was determined in order to understand the adsorption behavior of the GZ composites. Fig. S15 shows the adsorption data of Cu and Co ions by GZ composites at different time intervals. And the adsorption rate over the heavy metal ions was high as compared to the dye molecules over the ZnO NR and GZ7.5 nanocomposites (Fig. S16).

The kinetic data for the sorbent were fitted to a pseudo-first and second-order kinetic model and the calculated parameters from two kinetic models were listed in Table S1. The pseudo-second-order equation provides better correlation coefficient and agreement between calculated qe values. The results indicate that Cu (II) and Co (II) uptake onto GZ composites are favorable by the pseudo-second-order kinetic model and it reveals that the chemical adsorption can be well described with the pseudo-second-order kinetic model (Fig. S15b) [39].

3.5. Adsorption isotherms

The equilibrium adsorption isotherm was investigated in order to describe the interactive behavior between adsorbate and adsorbent, and also for designing adsorption systems [40]. Adsorption data were studied by Langmuir and Freundlich isotherm models
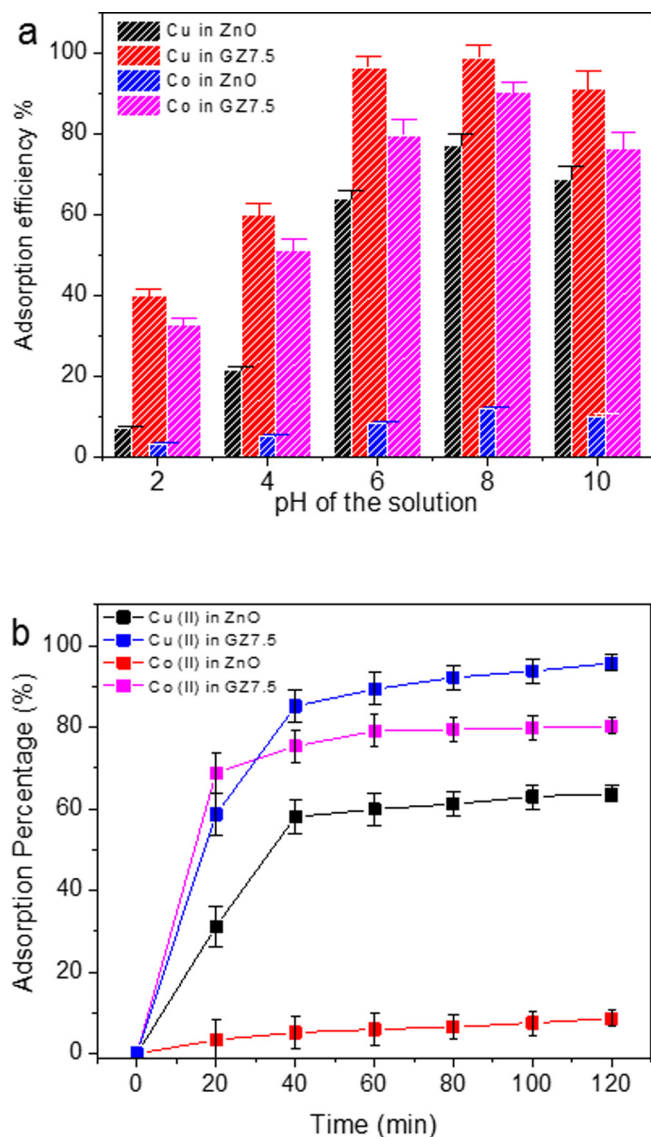
Table 1
Comparison of maximum adsorption capacities (mg/g) with various adsorbents for Cu (II) and Co (II).

Absorbents	Cu (II) mg/g^{-1}	Co (II) mg/g^{-1}	Ref
Nanometer TiO2	26.50		[44]
Kaolin	0.76	0.919	[45,46]
Functionalized MWCNT	6.64		[47]
Amine functionalize magnetic nano absorbent	12.43		[48]
GO–CS aerogel	25.4		[49]
Amination graphene oxide		116.35	[50]
Magnetite-reduced graphene oxide		0.71	[51]
G-ZnO	37.45		[10]
ZnO NR-rGO nanocomposites	67.39	36.35	This work

the ZnO NR-rGO nanocomposite, which proves the metal removal capability. The comparison of the maximum adsorption capacity of Cu (II), and Co (II) with various adsorbents is listed in Table S2. It can be seen that ZnO NR-rGO nanocomposite have a relatively large adsorption capacity of 67.399 and 36.354 mg/g for Cu (II) and Co (II) respectively, indicating that ZnO NR-rGO nanocomposite is a potential material for removal of Cu (II) and Co (II) from aqueous solutions. The Freundlich constant n is found to be greater than 1 which is a favorable condition for adsorption [43]. The maximum adsorption efficiency (Qo) observed based on Langmuir model was 67.399 mg/g for the ZnO NR-rGO nanocomposite with the correlation coefficient (R^2) of 0.9872 as shown in Fig. S17. Data fitted with Freundlich isotherm and the values of adsorption isotherm constants $1/n$ and R^2 are 0.1413 and 0.9083 respectively and the empirical parameter $1/n$ value is in the range $0.1 < 1/n < 1$ which confirms that the adsorption process is favourable [43].

The Freundlich isotherm is favourable for adsorption of Cu(II) and Co(II) ions from aqueous solution by ZnO NR-rGO nanocomposite and confirms their good heterogeneous adsorption capacity. The Cu (II) and Co (II) removal capacity of the ZnO NR-rGO nanocomposite was higher than that of the reported values as presented in Table 1. Interestingly, on coupling the heavy metal adsorption and degradation of dye molecules under visible irradiation, the heavy metal adsorbed catalysts exhibited pronounced degradation performance which is 1.7 times faster than the catalytic activity without the heavy metal ions (Fig. S19). The adsorbed heavy metal ions on the catalyst surface favour the effective photo generated carrier separation rate which enhanced the production of reactive oxygen species and fastened the degradation rate. The coupling effect of heavy metal adsorption and photodegradation properties and their advantage over the effective carrier separation will be further investigated in our future works. The ZnO NR-rGO nanocomposite provides large adsorption sites due to their high specific surface area and the rGO exhibits the high adsorption capacity due to the π-π interaction with the metal ions. Therefore, the adsorption capacities were relatively more and Cu (II) and Co (II) ions were easily adsorbed on the surface of the nanocomposites.

4. Conclusion

In summary, we successfully synthesized 1D ZnO NRs immobilized on rGO via hydrothermal process via anchoring ZnO NRs on rGO as an efficient catalyst for degradation and heavy metal adsorption. The reduction of GO during the hydrothermal process provided excellent dispersion in solution, thereby enabling uniform attachment of ZnO NRs along with their 1D axis without restacking of rGO. The unique attachment of the composite formation exhibited high catalytic degradation efficiency under visible light irradiation and stable dye and heavy metal adsorptive behav-

Fig. 9. (a) Effect of solution pH on the adsorption (Dosage of adsorbent = 10 mg, concentration of metal ions = 10 mg/L, contact time = 120 min.) (b) Effect of contact time on the adsorption of Cu (II), and Co (III) onto ZnO NR and GZ7.5 composites. (Dosage of adsorbent = 10 mg, concentration of metal ions = 10 mg/L, pH = 6.0).

when the initial metal ion concentrations ranged from 10 to 100 mg/L. The results obtained from the two adsorption isotherms are shown in Table S2. By comparing the R^2 values of both models, the Langmuir model was seen to fit the experimental data better, suggesting monolayer adsorption of Cu (II), and Co (II) onto the surface of the ZnO NR-rGO nanocomposite. Furthermore, the values of the dimensionless parameter, R_L, are between 0.0812 and 0.792 ($0 < R_L < 1$), which is consistent with the requirement for a favorable adsorption process [41]. The mapping and EDAX results reveal that the presence of Cu and Co ions over the GZ composite after adsorption concluded the adsorption of metal ions over the composite surface (Fig. S18). Mapping results from the Fig. S18 reveals the presence of Cu over the ZnO, indicating that the ZnO can absorb the Cu ions and while grafting the rGO with ZnO enhances the Cu metal ion absorption. This may be due to the strong electronegativity of Cu^{2+} ion that can bond with O atom over the ZnO nanostructures [42]. But this trend was not observed with the Co metal ions, and in this case, rGO plays the sole role for the adsorption process. We could see the extent of metal adsorption from the elemental distribution/mapping of Co and Cu over

ior compared to ZnO NRs. This was mainly attributed to (i) improved bifunctional catalytic activity; (ii) facile electron transport via rGO connected parallel with elongated 1D ZnO NRs; (iii) the high surface area of both rGO and ZnO NRs. Our synthesis strategy can be applied to diverse combinations using various types of catalytic metal oxides with reduced form of 2D GO. The unique morphological nature and complementary properties of the 1D metal oxide/2D carbon can open up new nanocomposite building blocks to develop highly efficient catalysts.

Acknowledgements

Appendix A. Supplementary data

Supplementary data associated with this article can be found, in the online version, at http://dx.doi.org/10.1016/j.cej.2017.05.105.

References

[1] J.T. Kim, M.H. Son, D.H. Lee, W.J. Seong, S. Han, Y.S. Chang, Partitioning behavior of heavy metals and persistent organic pollutants among feto-maternal bloods and tissues, Environ. Sci. Technol. 49 (2015) 7411–7422.

[2] H. Kuang, C. Xing, C. Hao, L. Liu, L. Wang, C. Xu, Rapid and highly sensitive detection of lead ions in drinking water based on a strip immunosensor, Sensors (Basel) 13 (2013) 4214–4224.

[3] P.Z. Raya, H.J. Shipley, Inorganic nano-adsorbents for the removal of heavy metals and arsenic: a review, RSC Adv. 5 (2015) 29885–29907.

[4] M. Hua, S. Zhang, B. Pan, W. Zhang, L. Lv, Q. Zhang, Heavy metal removal from water/wastewater by nanosized metal oxides: a review, J. Hazard. Mater. 211–112 (2012) 317–331.

[5] J. Li, J. Zhang, L. Fang, J. Wang, M. Shen, X. Su, Enhanced visible light photocatalytic properties of TiO_2 thin films on the textured multicrystalline silicon wafers, J. Mater. Chem. A 3 (2015) 4903–4908.

[6] Y. Wang, Q. Wang, X. Zhan, F. Wang, M. Safdar, J. He, Visible light driven type II heterostructures and their enhanced photocatalysis properties: a review, Nanoscale 5 (2013) 8326–8339.

[7] M. Ge, C. Cao, J. Huang, S. Li, Z. Chen, K.Q. Zhang, S.S. Al-Dey, Y. Lai, A review of one-dimensional TiO_2 nanostructured materials for environmental and energy applications, J. Mater. Chem. A 4 (2016) 6772–6801.

[8] A. Senthamizhan, A. Celebioglu, S. Bayir, M. Gorur, E. Doganci, F. Yilmaz, T. Uyar, Highly fluorescent pyrene-functional polystyrene copolymer nanofibers for enhanced sensing performance of TNT, ACS Appl. Mater. Interfaces 7 (2015) 21038–21046.

[9] Y. Liu, Y. Ma, C. Liu, Z. Zhang, W. Yang, S. Nie, X. Zhou, The effective removal of Cr(VI) ions by carbon dot-silica hybrids driven by visible light, RSC Adv. 6 (2016) 68530–68537.

[10] A. Cazetta, O. Pezoti, K.C. Bedin, T.L. Silva, A.P. Junior, T. Asefa, V.C. Almeida, Magnetic activated carbon derived from biomass waste by concurrent synthesis: efficient adsorbent for toxic dyes, ACS Sustainable Chem. Eng. 4 (2016) 1058–1068.

[11] Y. Zhu, S. Murali, W. Cai, X. Li, J.W. Suk, J.R. Potts, R.S. Ruoff, Graphene and graphene oxide: synthesis and properties and application, Adv. Mater. 22 (2010) 3906–3924.

[12] X. Xie, K. Kretschmera, G. Wang, Advances in graphene-based semiconductor photocatalysts for solar energy conversion: fundamentals and materials engineering, Nanoscale 7 (2015) 13278–13292.

[13] C.L. Chen, J. Hu, D.D. Shao, J.X. Li, X.K. Wang, Adsorption behavior of multiwall carbon nanotube/iron oxide magnetic composites for Ni(II) and Sr(II), J. Hazard. Mater. 164 (2009) 923–928.

[14] W.H. Ryu, T.H. Yoon, S.H. Song, S. Jeon, Y.J. Park, I.D. Kim, Bifunctional composite catalysts using Co_3O_4 nanofibers immobilized on nonoxidized graphene nanoflakes for high-capacity and long-cycle Li–O_2 batteries, Nano Lett. 13 (2013) 4190–4197.

[15] H.D. Lim, K.Y. Park, H. Song, E.Y. Jang, H. Gwon, J. Kim, Y.H. Kim, M.D. Lima, R. Ovalle Robles, X. Lepro, R.H. Baughman, K. Kang, Enhanced power and rechargeability of a Li–O_2 battery based on a hierarchical-fibril CNT electrode, Adv. Mater. 25 (2013) 1348–1352.

[16] P. Manivel, M. Dhakshnamoorthy, A. Balamurugan, N. Ponpandian, D. Mangalaraj, C. Viswanathan, Conducting polyaniline-graphene oxide fibrous nanocomposites: preparation, characterization and simultaneous

[17] electrochemical detection of ascorbic acid, dopamine and uric acid, RSC Adv. 3 (2013) 14428–14437.

[17] K.S. Ranjith, R. Pandian, E. McGlynn, R.T. Rajendra Kumar, Alignment, morphology and defect control of vertically aligned ZnO nanorod array: competition between "surfactant" and "stabilizer" roles of the amine species and its photocatalytic properties, Cryst. Growth Des. 14 (2014) 2873–2879.

[18] J. Jiaa, A. Wua, S. Luan, Spectrometry recognition of polyethyleneimine towards heavy metal ions, Colloids Surf., A 449 (2014) 1–7.

[19] A. Ghosh, S. Shukla, G.S. Khosla, B. Lochab, S. Mitra, Sustainable sulfur-rich copolymer/graphene composite as lithium-sulfur battery cathode with excellent electrochemical performance, Sci Rep. 6 (2016) 25207.

[20] R. Das, A. Kumar, Y. Kumar, S. Sen, P.M. Shirage, Effect of growth temperature on the optical properties of ZnO nanostructures grown by simple hydrothermal method, RSC Adv. 5 (2015) 60365–60372.

[21] N.R. Wilson, P.A. Pandey, R. Beanland, R.J. Young, I.A. Kinloch, L. Gong, Z. Liu, K. Suenaga, J.P. Rourke, S.J. York, J. Sloan, Graphene oxide: structural analysis and application as a highly transparent support for electron microscopy, ACS Nano 3 (2009) 2547–2556.

[22] A. Calzolari, M.B. Nardelli, Dielectric properties and Raman spectra of ZnO from a first principles finite-differences/finite-fields approach, Sci Rep. 3 (2013) 2999.

[23] J.Y. Li, H. Li, Physical and electrical performance of vapor-solid grown ZnO straight nanowires, Nanoscale Res. Lett. 4 (2009) 165–168.

[24] X.Y. Ye, Y.M. Zhou, Y.Q. Sun, J. Chen, Z.Q. Wang, Preparation and characterization of Ag/ZnO composites via a simple hydrothermal route, J. Nanopart. Res. 11 (2009) 1159–1166.

[25] T. Pandiyarajan, R.V. Mangalaraja, B. Karthikeyan, S.S. Guzman, H.D. Mansilla, D. Contreras, N. Escalona, M.A.G. Pinilla, Microstructure, vibrational and visible emission properties of low frequency ultrasound (42 kHz) assisted ZnO nanostructures, RSC Adv. 6 (2016) 20437–20446.

[26] M.K. Kavitha, H. John, P. Gopinath, R. Philip, Synthesis of reduced graphene oxide–ZnO hybrid with enhanced optical limiting properties, J. Mater. Chem. C 1 (2013) 3669–3676.

[27] F. Kayaci, S. Vempati, I. Donmez, N. Biyikli, T. Uyar, Role of zinc interstitials and oxygen vacancies of ZnO in photocatalysis: a bottom-up approach to control defect density, Nanoscale 6 (2014) 10224–10234.

[28] A. Senthamizhan, B. Balusamy, Z. Aytac, T. Uyar, Grain boundary engineering in electrospun ZnO nanostructures as promising photocatalysts, Cryst. Eng. Commun. 18 (2016) 6341–6351.

[29] A. Janotti, C.G. Van de Walle, Native point defects in ZnO, Phys. Rev. B. 76 (2007) 165202.

[30] D.I. Son, B.W. Kwon, D.H. Park, W.S. Seo, Y. Yi, B. Angadi, C.L. Lee, W.K. Choi, Emissive ZnO-graphene quantum dots for white-light-emitting diodes, Nat. Nanotechnol. 7 (2012) 465–471.

[31] F.L. Kuo, Y. Li, M. Solomon, J. Du, N.D. Shepherd, Workfunction tuning of zinc oxide films by argon sputtering and oxygen plasma: an experimental and computational study, J. Phys. D: Appl. Phys. 45 (2012) 065301–065307.

[32] C. Tao, J. Wang, S. Qin, Y. Lv, Y. Long, H. Zhu, Z. Jiang, Fabrication of pH-sensitive graphene oxide-drug supramolecular hydrogels as controlled release systems, J. Mater. Chem. 22 (2012) 24856–24861.

[33] Y.C. Chena, K. Katsumata, Y.H. Chiua, K. Okada, N. Matsushita, Y.J. Hsua, ZnO-graphene composites as practical photocatalysts for gaseous acetaldehyde degradation and electrolytic water oxidation, Appl. Catal. A 490 (2015) 1–9.

[34] T. Lv, L. Pan, X. Liu, T. Lu, G. Zhu, Z. Sun, Enhanced photocatalytic degradation of methylene blue by ZnO-reduced graphene oxide composite synthesized via microwave-assisted reaction, J. Alloys Compd. 509 (2011) 10086–10091.

[35] S. Vadivel, D. Maruthamani, B. Paul, S.S. Dhar, H.A. Yangjeh, S. Balachandran, B. Saravanakumar, A. Selvakumar, K. Selvam, Biomolecule-assisted solvothermal synthesis of Cu_2SnS_3 flowers/RGO nanocomposites and their visible-light-driven photocatalytic activities, RSC Adv. 6 (2016) 74177–74185.

[36] X. Zhang, T. Peng, S. Song, Recent advances in dye-sensitized semiconductor systems for photocatalytic hydrogen production, J. Mater. Chem. A 4 (2016) 2365–2402.

[37] G.K. Pradhan, D.K. Padhi, K. Parida, Fabrication of α-Fe_2O_3 nanorod/RGO composite: a novel hybrid photocatalyst for phenol degradation, ACS Appl. Mater. Interfaces 5 (2013) 9101–9110.

[38] N. Badr, K.A. Al-Qahtani, Treatment of wastewater containing arsenic using Rhazya stricta as a new adsorbent, Environ. Monit. Assess. 185 (2013) 9669–9681.

[39] K. Vasanth Kumar, Linear and non-linear regression analysis for the sorption kinetics of methylene blue onto activated carbon, J. Hazard. Mater. B 137 (2006) 1538–1544.

[40] A. Afkhami, R. Moosavi, Adsorptive removal of Congo Red, a carcinogenic textile dye, from aqueous solutions by maghemite nanoparticles, J. Hazard. Mater. 174 (2010) 398–403.

[41] W.C. Wanyonyi, J.M. Onyari, P.M. Shiundu, Adsorption of Congo Red Dye from aqueous solutions using roots of Eichhornia crassipes: kinetic and equilibrium studies, Energy Procedia 50 (2014) 862–869.

[42] S. Mahdavi, M. Jalali, A. Afkhami, Removal of heavy metals from aqueous solutions using Fe_3O_4, ZnO, and CuO nanoparticles, J. Nanopart. Res. 14 (2012) 846.

[43] A.O. Dada, A.P. Olalekan, A.M. Olatunya, O. Dada, Langmuir, Freundlich, Temkin and Dubinin-Radushkevich, isotherms studies of equilibrium sorption of Zn2+ unto phosphoric acid modified rice husk, IOSR J. Appl. Chem. 3 (2012) 38–45.

[44] S. Qian, S. Zhang, Z. Huang, M. Xiao, F. Huang, Preconcentration of ultra-trace copper in water samples with nanometer-size TiO_2 colloid and determination by GFAAS with slurry sampling, Microchim. Acta 166 (2009) 251–254.

[45] V. Chantawong, N.W. Harvey, V.N. Bashkin, Comparison of heavy metal adsorptions by Thai Kaolin and Ballclay, Water Air Soil Pollut. 148 (2003) 111–125.

[46] O. Yavuz, Y. Altunkaynak, F. Güzel, Removal of copper, nickel, cobalt and manganese from aqueous solution by kaolinite, Water Res. 37 (2003) 948–952.

[47] J. Wang, X. Ma, G. Fang, M. Pan, X. Ye, S. Wang, Preparation of iminodiacetic acid functionalized multi-walled carbon nanotubes and its application as sorbent for separation and preconcentration of heavy metal ions, J. Harzard. Mater. 186 (2011) 1985–1992.

[48] S.H. Huang, D.H. Chen, Rapid removal of heavy metal cations and anions from aqueous solutions by an amino-functionalized magnetic nano-adsorbent, J. Harzard. Mater. 163 (2009) 174–179.

[49] B. Yu, J. Xu, J.H. Liu, S.T. Yang, J. Luo, Q. Zhou, J.W.R. Liao, H. Wang, Y. Liu, Adsorption behavior of copper ions on graphene oxide–chitosan aerogel, J. Environ. Chem. Eng. 1 (2013) 1044–1050.

[50] F. Fang, L. Kong, J. Huang, S. Wu, K. Zhang, X. Wang, B. Sun, Z. Jin, J. Wang, X. Huang, J. Liu, Removal of cobalt ions from aqueous solution by an amination graphene oxide nanocomposite, J. Hazard. Mater. 270 (2014) 1–10.

[51] A. Tayyebi, M. Outokesh, Supercritical synthesis of a magnetite-reduced graphene oxide hybrid with enhanced adsorption properties toward cobalt & strontium ions, RSC Adv. 6 (2016) 13898–13913.